Supporting Information:

Low Thermal Conductivity in Franckeite

Heterostructures

Jean Spiece,[†,‡] Sara Sangtarash,[¶] Marta Mucientes,[†] Aday J. Molina-Mendoza,[§]

Kunal Lulla,[†] Thomas Mueller,[§] Oleg Kolosov,[*,†] Hatef Sadeghi,[*,¶] and

Charalambos Evangeli[*,‖,†]

[†]*Physics Department, Lancaster University, Lancaster LA1 4YW, United Kingdom*

[‡]*Institute of Condensed Matter and Nanosciences, Université Catholique de Louvain, 1348*
Louvain-la-Neuve, Belgium

[¶]*Device Modelling Group, School of Engineering, University of Warwick, CV4 7AL*
Coventry, United Kingdom

[§]*Vienna University of Technology, Gusshausstrasse 27-29, Vienna A-1040, Austria*

[‖]*Department of Materials, University of Oxford, Oxford OX1 3PH, United Kingdom*

E-mail: o.kolosov@lancaster.ac.uk; Hatef.Sadeghi@warwick.ac.uk; ch.evangeli@gmail.com

Contents

3 Diffusive thermal transport model   **S-7**

4 Computational Methods   **S-12**

5 Sample Fabrication   **S-15**

References   **S-16**

1 Scanning Thermal Microscopy

1.1 Lateral resolution

In FigureS1 a and b the topography and the corresponding thermal resistance image are shown as acquired simultaneously. We estimate the thermal lateral resolution from thermal resistance profiles with two signal levels corresponding to 3 and 4 layers of Franckeite. As a resolution criterion, we use the $10 - 90\%$ of the lateral distance of this change. We find lateral resolution varying from $37 - 48$nm. Thus the tip radius is between 74 and 96nm (see Figure S1 d).
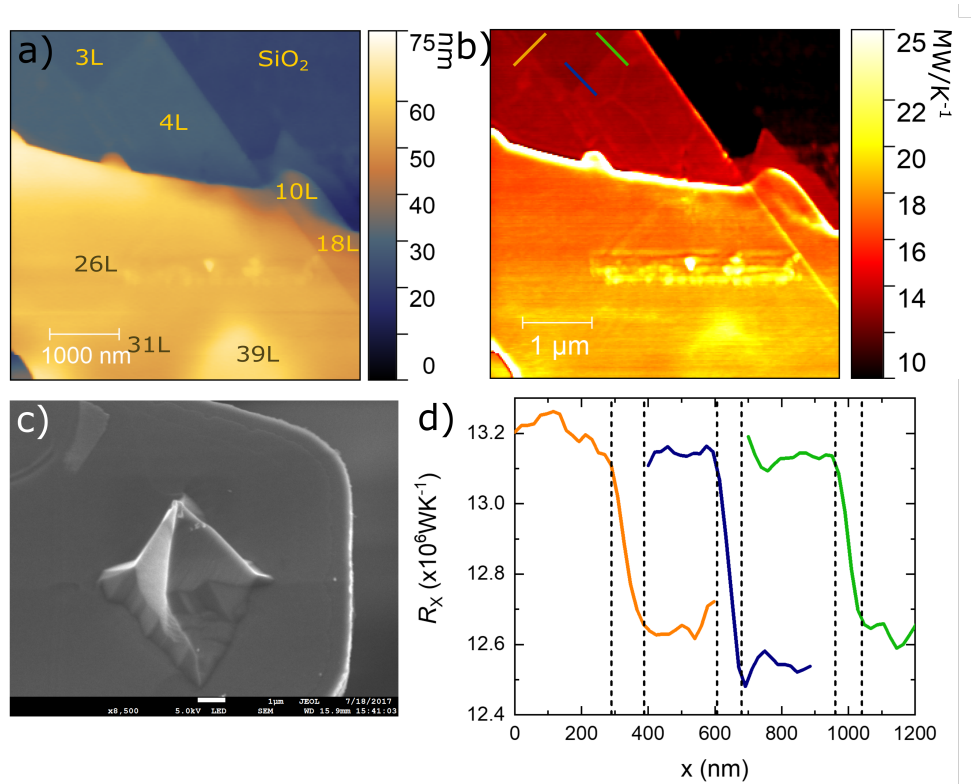

Figure S1: (a,b) Topography (a) and Thermal Resistance (b) images acquired simultaneously in high vacuum at $T_{\text{sample}} = 156$K. (c) SEM image of the tip used for the experiments (d)Thermal resistance profiles obtained from the thermal resistance image (in image (b) the lines where the profiles were taken are shown with the corresponding color) With dotted lines is the $10 - 90\%$ (96, 74, 80nm) of the lateral distance where thermal resistance changes between 3 and 4 layers of franckeite.

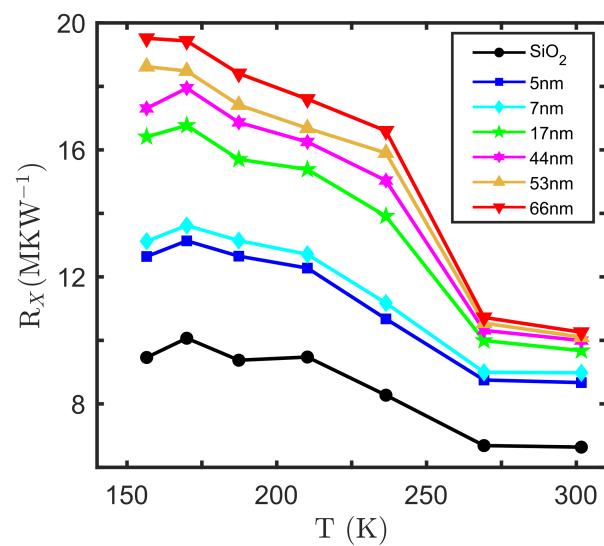## 1.2 Thermal resistance with temperature

Figure S2: Thermal resistance R_X as a function of temperature for the different thickness areas of franckeite sample.
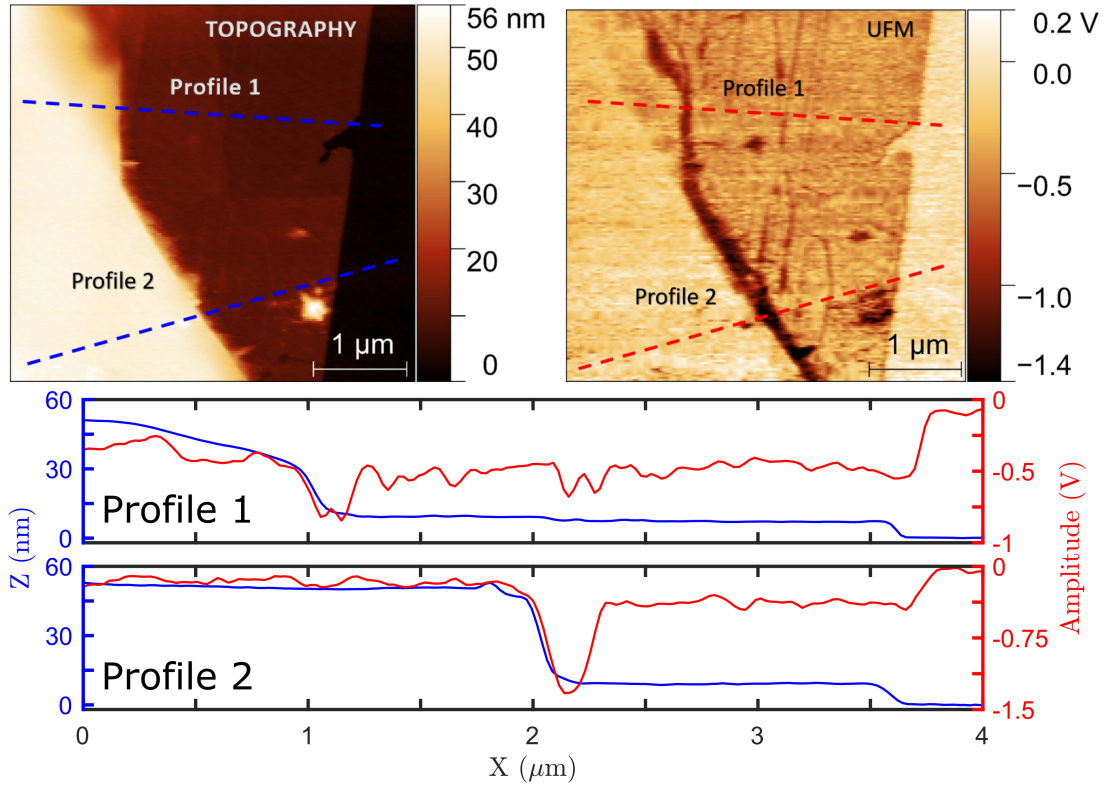
2 Ultrasonic Force Microscopy

Figure S3: (a,b) Topography (a) and UFM (b) images acquired simultaneously. With dashed lines the profiles plotted at (c) and (d) are shown. (c,d) Two different profiles of topography (blue) and UFM-amplitude (red).

To probe the nanomechanical properties of franckeite we use Ultrasonic Force Microscopy (UFM), an AFM based technique which is shown to be highly sensitive to surface and subsurface structures of 2D-materials.[S1,S2] Areas with few layers, appear darker meaning that are of lower stiffness whereas thicker areas and SiO_2 are brighter, therefore of higher stiffness. The profiles of the topography and UFM images (see Figure S3 c and d) show an increase of stiffness with the thickness with the thicker areas being slightly less stiff than the SiO_2 substrate. UFM is sensitive to the features beneath 2D materials, and this phenomena can be attributed to the probing of the non-uniform adhesion between the franckeite film and the substrate as a consequence of the corrugations present on the substrate surface, which

affects the adhesion uniformity of the flake. The thick part of the franckeite present a stiffness comparable with the substrate value. In this case, the flake is excessively thick for the UFM sensing to the characteristic of the substrate-flake interface. Therefore, the contact stiffness is determined by the bulk stiffness of franckeite.

3 Diffusive thermal transport model

We express the thermal SThM measured resistance as a sum of resistances: $R_X = R_t + R_{int} + R_s$, where R_t is the SThM tip thermal resistance, R_{int} the tip-franckeite thermal boundary resistance and R_s is the sample spreading resistance. We estimate R_t out of the franckeite free SiO_2 area (see SI) and express express R_{int} as $R_{int}/\pi\rho^2$, where R_{int} is the SiO_2-franckeite interface thermal resistivity and ρ is the tip radius which we obtained from the thermal images and SEM imaging of the SThM tip (see Supporting Information note 1). R_s of a layered material on a substrate is expressed as a function of the layer thickness and the thermal conductivities of the substrate and the material.[S3–S6] Since the thermal conductivity of SiO_2 is known,[S7] R_X is determined by the only remaining unknowns: k_l and R_{int}. We also account for thermal transport anisotropy and we define k_c and k_i for the cross-plane and in-plane thermal conductivity, respectively. For very thin areas (10 layers) compared to the tip diameter (80nm), the heat flow from the tip to the substrate is almost vertical[S8] and we use an isotropic model with $k_l = k_c$ and r_{int} as fitting parameters. For thicker areas this assumption is not valid and we use an orthotropic model considering both k_c and k_i (see Experimental section and Supporting Information note 3 for more details on the modeling procedure).

In more detail, the measured thermal resistance can be divided in three resistances in series:

$$R_m = R_{tip} + R_{(tip-sample)} + R_{spr} \tag{1}$$

R_{tip} and $R_{tip-sample}$ can be assumed to be non-thickness dependent. To obtain the tip thermal resistance R_{tip}, we subtracted from the measurement of the silicon oxide substrate the spreading resistance of the oxide and the oxide-oxide tip sample resistance. The values of R_{tip} obtained lie between 2 and 4.5 $\times 10^6$ KW^{-1}. Those values are in good agreement with values reported elsewhere.[S4,S9]

$R_{tip-sample}$ can be written as $r_{int}/\pi p^2$ where r_{int} is the silicon oxide-franckeite contact

resistivity and p is the probe contact radius (40 nm in our case – as estimated by SEM and image analysis). r_{int} is unknown and will be used as a fitting parameter later.

The spreading resistance R_{spr} for a layer on substrate is a function of the thickness t_{eff} and layer and substrate thermal conductivities, k_{layer} and k_{sub}.[S3,S4] As the substrate is silicon oxide, its thermal conductivity is known across a wide temperature range [REF]. To include the resistivity between the layer and the substrate t_{eff} is defined as : $t_{eff} = t + r_{int}k_{layer}$ Where t is the physical thickness. The analytical expression giving the thermal spreading resistance, R_{spr}, is given by:[S3]

$$R_{spr}(t) = \frac{1}{\pi k_{layer} a} \int_0^\infty \left[\frac{1 + K \exp\left(\frac{-2\xi t_{eff}}{a}\right)}{1 - K \exp\left(\frac{-2\xi t_{eff}}{a}\right)} \right] J_1(\xi) \sin(\xi) \frac{d\xi}{\xi^2} \tag{2}$$

With $K = \frac{1 - k_{sub}/k_{layer}}{1 + k_{sub}/k_{layer}}$.

However, this expression is valid for an isotropic material and does not account for any anisotropy that could arise in 2D materials. In 2D materials, we can usually define $k_\perp$ and $k_\parallel$ as the cross-plane and in-plane thermal conductivities. Such a system, symmetric along the vertical axis, is called orthotropic. The equation for the spreading resistance given above can include both in-plane and cross-plane conductivities by performing the following transformation:[S10]

$$k_{layer} \rightarrow \sqrt{\left(\frac{k_\perp}{k_\parallel}\right)} \tag{3}$$

$$t_{eff} \rightarrow \sqrt{\frac{k_\parallel}{k_\perp}} t + r_{int}k_{layer} \tag{4}$$

The final fitting equation is thus:

$$R_m = R_{tip} + r_{int}/\pi p^2 + R_{spr}(t) \tag{5}$$

This equation contains three fitting parameters, r_{int}, $k_\parallel$, $k_\perp$.

We performed the fitting in two steps. First, we assume that in extremely thin layers most

of the thermal transport is vertical. This is supported by the comparison between the layer thickness of few nanometers and the probe diameter around 80 nm. With this assumption, we fitted the smallest layers with an isotropic model, disregarding any anisotropy. The results of this fit are the parameters r_{int} and $k_\perp$. Using those results, we then input them as parameters to fit thicker layers with the only fitting parameters being then $k_\parallel$.

As a results of this process, we obtained the three parameters r_{int}, $k_\parallel$, $k_\perp$.

Another possibility of fitting process is to have the same two steps but instead of using both parameters r_{int} and $k_\perp$ as inputs for the second fitting step, just using r_{int} as input and fit $k_\perp$, $k_\parallel$.

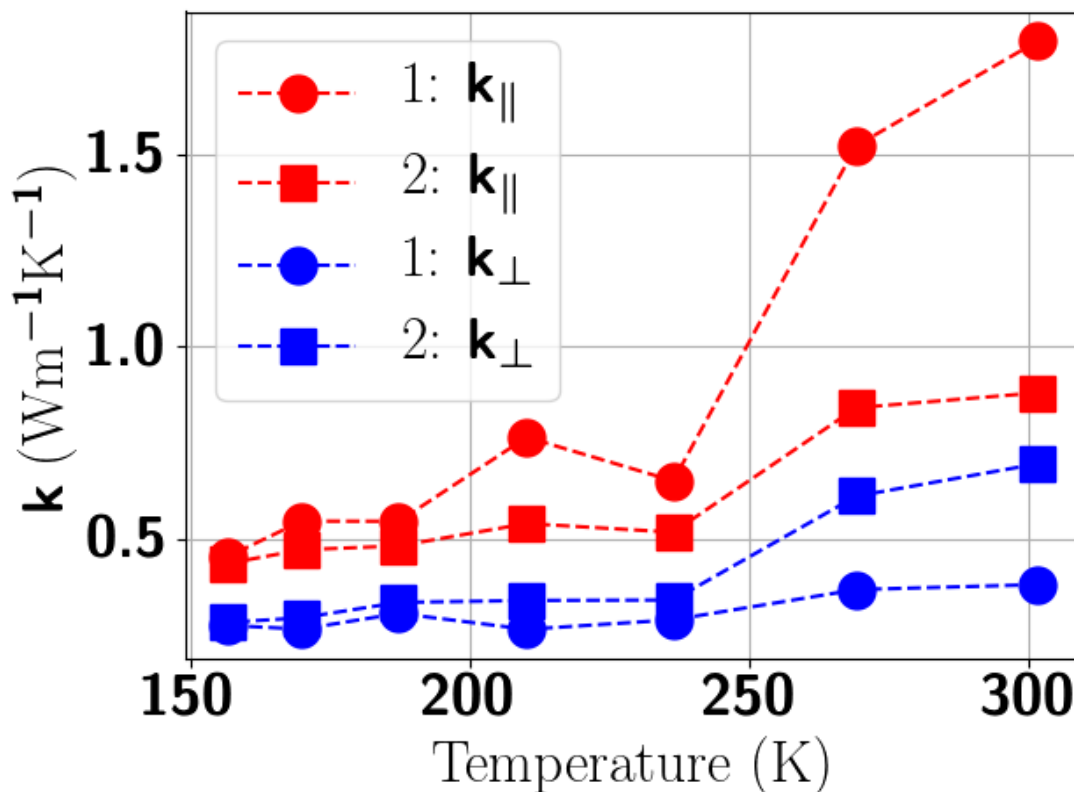The results of this second fitting method are displayed in Figure S4.

Figure S4: Fitting results of the two possible methods. In the first method (1 - circles), we first fit thin layers of Franckeite with the isotropic model and obtained r_{int} and $k_\perp$. From these results, we then used r_{int} to fit thick layers with the orthotropic model to obtain $k_\perp$ and $k_\parallel$. In the second method (2 - squares), we used r_{int} and $k_\perp$ for fitting the orthotropic model to thick layers and obtained $k_\parallel$.

Finally, as our thermal conductivity's results come from a non-linear fitting method, it is not straight forward to deduct the error on these quantities. We thus consider that the errors of our measurements propagates to the thermal conductivities results. For each temperature, we have thermal resistance measurement error. We chose the highest error of that set of measurements, normalised and applied it to the corresponding thermal conductivity.

We can then evaluate our model and fitting method by considering the worst cases in the thermal conductivity values. Taking minimal and maximal values and plugging them into our orthotropic model shows us (Figure S6) that our findings lie in a realistic range.
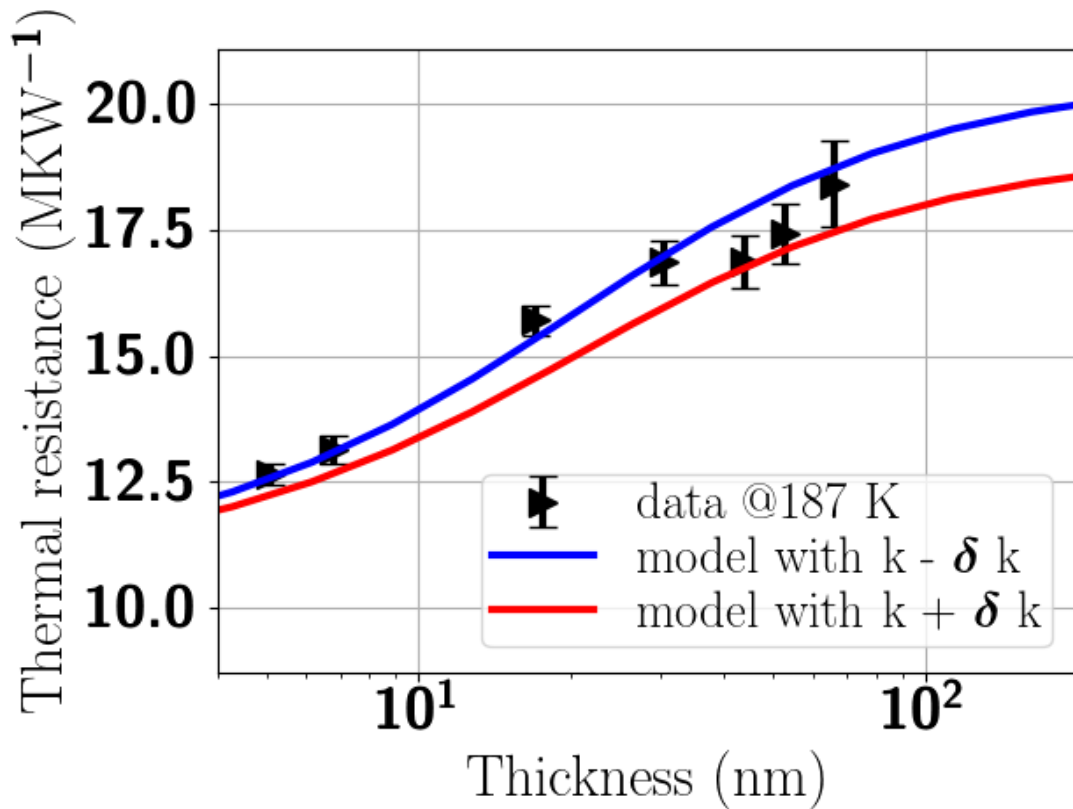

Figure S5: Comparison between the minimal and maximal values of thermal conductivity's used in the orthotropic model compared to the experimental data for $T = 187$K.
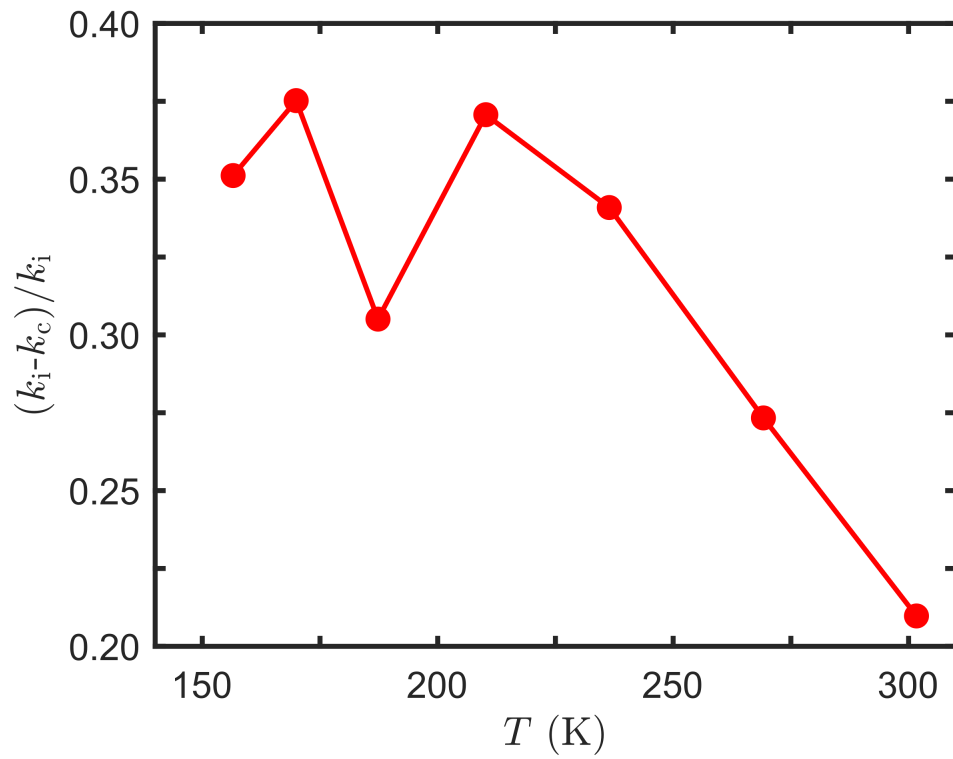
Figure S6: Relative change of thermal conductivity with temperature. The anisotropy is decreasing with temperature possibly due to activation of some phonon modes

4 Computational Methods

4.1 Geometry optimization

The geometry optimisation of franckeite unit cell was performed using the SIESTA[S11] implementation of density functional theory (DFT), to the force tolerance of 10 meV/Å with a double- polarized basis set (DZP) and the Generalized Gradient Approximation (GGA) functional with Perdew-Burke-Ernzerhof (PBE) parameterization. A real-space grid was defined with an equivalent energy cut-off of 350 Ry.

4.2 Phonon dispersion relation

From the optimised unit cell geometry of franckeite, we construct a super-cell shown in figure 1a and construct dynamical matrix as described below for each supper-cell (k_0) as well as coupling matrix elements (K_1) to the neighbouring cell in H/Q/H/Q configuration (see Figure 1a). We then calculate phonon dispersion relation using these k_0 and k_1 and the method described in.[S12]

4.3 Phonons transport and thermal conductivity

Following the method described in[S12][S13][S14] each atom was displaced from the relaxed optimised position in the positive and negative x, y and z directions with $0.01 Å$. For each displacement, the forces F in three directions on all atoms were then calculated and used to construct the dynamical matrix D=K/M where the mass matrix M and Hessian matrix K obtained from finite differences. To satisfy momentum conservation, the diagonal terms in K is calculated by negative of sum of off-diagonal terms. The phonon transmission then can be calculated from the relation $T_p = Trace(\Gamma_L(\omega)G(\omega)\Gamma_R(\omega)G^\dagger(\omega))$ where $\Gamma_{L,R} = i(\sum_{L,R}(\omega) - \sum_{L,R}^\dagger(\omega))$ describes the level broadening due to the coupling to the left L and right R electrodes, $\sum_{L,R}(\omega)$ are the retarded self-frequencies associated with this coupling and $G = (\omega^2 I - D - \sum_L - \sum_R)^{-1}$ is the retarded Green's function, where D and

I are the dynamical and the unit matrices, respectively. The phonon thermal conductivity κ_p at temperature T is then calculated from $\kappa_p(T) = \hbar/2\pi \int_0^\infty \omega T_p(\omega)(\partial f/\partial T)$ where $f = 1/(e^{\hbar\omega/k_B T} - 1)$ is Bose–Einstein distribution function and and k_B are reduced Planck's and Boltzmann's constants, respectively.

4.4 Electron transport

To calculate electronic properties of the device formed by franckeite, from the converged DFT calculation, the underlying mean-field Hamiltonian H was combined with our quantum transport code, Gollum[S12].[S13] This yields the transmission coefficient for electrons of energy E (passing from the source to the drain) via the relation $T = Trace(\Gamma_L(E)G(E)\Gamma_R(E)G^\dagger(E))$ where $\Gamma_{L,R} = i(\sum_{L,R}(E) - \sum_{L,R}^\dagger(E))$ describes the level broadening due to the coupling between left L and right R electrodes and the central scattering region, $\sum_{L,R}(E)$ are the retarded self-energies associated with this coupling and $G = (E - H - \sum_L - \sum_R)^{-1}$ is the retarded Green's function, where H is the Hamiltonian and S is the overlap matrix obtained from SIESTA implementation of DFT.

4.5 Thermoelectric properties

The electronic contribution of the thermal conductance $\kappa_e = (L_0 L_2 - L_1^2)/hTL_0$ and the Seebeck coefficient $S = L_1/eTL_0$ are calculated from the electron transmission coefficient T(E) where the momentums $L_n = \int dE(E - E_F)^n(-\partial f_d/\partial E)$ and $f_d = (e^{((E-E_F)/k_B T)} + 1)^{-1}$ is the Fermi-Dirac probability distribution function, T is the temperature, E_F is the Fermi energy, e is electron charge and h is the Planck's constant.

4.6 Tight Binding Model

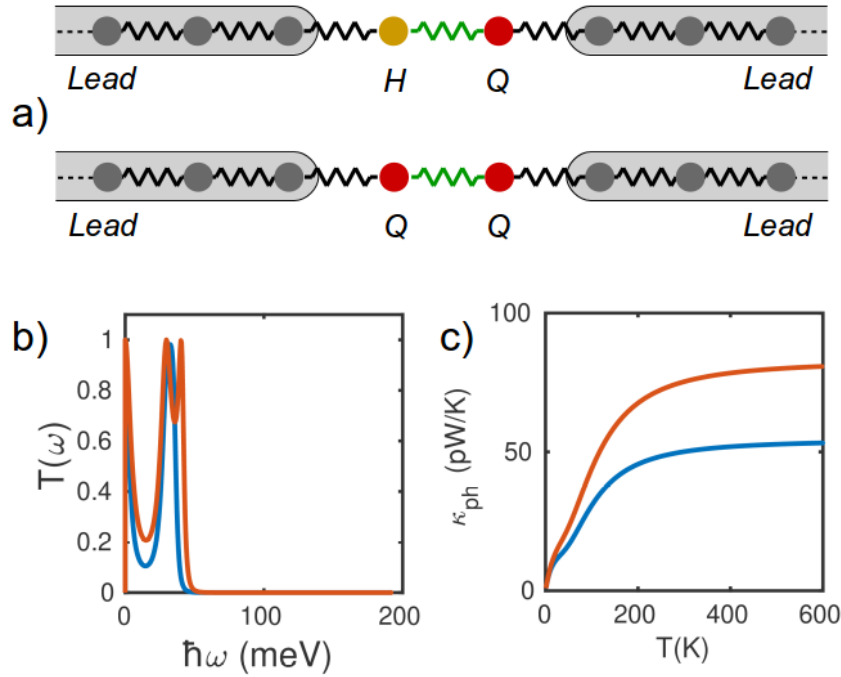## 4.7 Device structure for DFT calculations

Figure S7: Tight binding model. (a) two level systems representing Q and H layers where two ball is connected to a spring constant to each other and to two 1D semi-infinite lead of ball and springs, (b) Transmission probability Tp for phonons with energies $\hbar\omega$ and (c) thermal conductance when the spring constant between the levels are different.
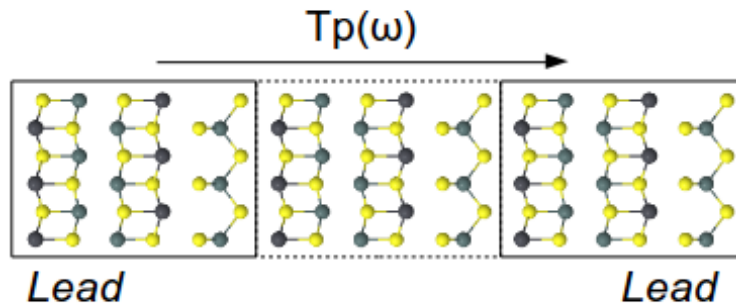

Figure S8: Device structure for DFT calculations. The figure shows the super-cell for phonon band structure calculations (boxes shown with black lines) and device structure consist of franckeite leads connected to franckeite scattering region. The phonon transport $T_p(\omega)$ through such a structure is equal to the number of open phonon conduction channels shown in figure 3 of the main text.

5   Sample Fabrication

Few-layer franckeite flakes are exfoliated from bulk material and transferred on a SiO2 substrate thermally grown on a Si wafer. The bulk franckeite material (San Jose Mine, Oruro City, Bolivia) is first scratched with a scalpel on an adhesive tape, resulting in thin chips of material. These chips are then thinned-down by repeatedly bringing the tape in contact with itself and peeling it off. Once a significant amount of thin material is obtained, a polydimethylsiloxane (PDMS) stamp is used to exfoliate franckeite from the adhesive tape. Transmission-mode optical microscopy is then employed to identify the thin flakes prior transfer on the SiO2/Si substrate (as described by Castellanos-Gomez et al.[S15]).

References

(S1) Kolosov, O.; Yamanaka, K. Nonlinear detection of ultrasonic vibrations in an atomic force microscope. *Japanese journal of applied physics* **1993**, *32*, L1095.

(S2) Robinson, B. J.; Giusca, C. E.; Gonzalez, Y. T.; Kay, N. D.; Kazakova, O.; Kolosov, O. V. Structural, optical and electrostatic properties of single and few-layers MoS2: effect of substrate. *2D Materials* **2015**, *2*, 015005.

(S3) Yovanovich, M. M.; Culham, J. R.; Teertstra, P. Analytical modeling of spreading resistance in flux tubes, half spaces, and compound disks. *IEEE Transactions on Components, Packaging, and Manufacturing Technology: Part A* **1998**, *21*, 168–176.

(S4) Menges, F.; Riel, H.; Stemmer, A.; Dimitrakopoulos, C.; Gotsmann, B. Thermal transport into graphene through nanoscopic contacts. *Physical review letters* **2013**, *111*, 205901.

(S5) Hwang, G.; Kwon, O. Measuring the size dependence of thermal conductivity of suspended graphene disks using null-point scanning thermal microscopy. *Nanoscale* **2016**, *8*, 5280–5290.

(S6) Sadeghi, M. M.; Park, S.; Huang, Y.; Akinwande, D.; Yao, Z.; Murthy, J.; Shi, L. Quantitative scanning thermal microscopy of graphene devices on flexible polyimide substrates. *Journal of Applied Physics* **2016**, *119*, 235101.

(S7) Anis-ur Rehman, M.; Maqsood, A. Measurement of thermal transport properties with an improved transient plane source technique. *International journal of thermophysics* **2003**, *24*, 867–883.

(S8) Feser, J. P.; Cahill, D. G. Probing anisotropic heat transport using time-domain thermoreflectance with offset laser spots. *Review of Scientific Instruments* **2012**, *83*, 104901.

(S9) Evangeli, C.; Spiece, J.; Sangtarash, S.; Molina-Mendoza, A. J.; Mucientes, M.; Mueller, T.; Lambert, C.; Sadeghi, H.; Kolosov, O. Nanoscale Thermal Transport in 2D Nanostructures from Cryogenic to Room Temperature. *Advanced Electronic Materials* **2019**, *5*, 1900331.

(S10) Muzychka, Y. S. Spreading Resistance in Compound Orthotropic Flux Tubes and Channels with Interfacial Resistance. *Journal of Thermophysics and Heat Transfer* **2014**, *28*, 313–319.

(S11) Soler, J. M.; Artacho, E.; Gale, J. D.; García, A.; Junquera, J.; Ordejón, P.; Sánchez-Portal, D. The SIESTA method for ab initio order-N materials simulation. *Journal of Physics: Condensed Matter* **2002**, *14*, 2745.

(S12) Sadeghi, H. Theory of Electron, Phonon and Spin Transport in Nanoscale Quantum Devices. *Nanotechnology* **2018**, *29*, 373001.

(S13) Ferrer, J.; et al., GOLLUM: a next-generation simulation tool for electron, thermal and spin transport. *New Journal of Physics* **2014**, *16*, 093029.

(S14) Sadeghi, H.; Sangtarash, S.; Lambert, C. Cross-plane enhanced thermoelectricity and phonon suppression in graphene/MoS2 van der Waals heterostructures. *2D Materials* **2016**, *4*, 015012.

(S15) Castellanos-Gomez, A.; Buscema, M.; Molenaar, R.; Singh, V.; Janssen, L.; Van Der Zant, H. S.; Steele, G. A. Deterministic transfer of two-dimensional materials by all-dry viscoelastic stamping. *2D Materials* **2014**, *1*, 011002.